Simultaneous Polar and Cluster Observations in the Northern and Southern Middle-Altitude Polar Cusps Around Equinox

F. Pitout, Aurélie Marchaudon, K. Trattner, J. Berchem, H. Laakso, C. Escoubet

JGR Space Physics

RESEARCH ARTICLE
10.1029/2020JA028346

Special Section:
Cluster 20th Anniversary: Results from the First 3D Mission

Simultaneous Polar and Cluster Observations in the Northern and Southern Middle-Altitude Polar Cusps Around Equinox

F. Pitout[1], A. Marchaudon[1], K. J. Trattner[2], J. Berchem[3], H. Laakso[4], and C. P. Escoubet[4]

[1]IRAP, Université de Toulouse 3/CNES/CNRS, Toulouse, France, [2]Laboratory for Atmospheric and Space Physics, University of Colorado Boulder, Boulder, CO, USA, [3]Department of Physics and Astronomy, University of California, Los Angeles, CA, USA, [4]ESA/ESTEC, Noordwijk, The Netherlands

Key Points:
- Data from Cluster and Polar show a symmetry in ion injections in the magnetospheric cusps
- Signatures corresponding to a single reconnection line running along the subsolar magnetopause and pulsed reconnection are highlighted
- Differences in convection velocities are found and ascribed to the effect of the tilt angle

Correspondence to:
F. Pitout,
frederic.pitout@irap.omp.eu

Citation:
Pitout, F., Marchaudon, A., Trattner, K. J., Berchem, J., Laakso, H., & Escoubet, C. P. (2020). Simultaneous Polar and Cluster observations in the northern and southern middle-altitude polar cusps around equinox. *Journal of Geophysical Research: Space Physics*, *125*, e2020JA028346. https://doi.org/10.1029/2020JA028346

Received 12 JUN 2020
Accepted 23 OCT 2020
Accepted article online 11 NOV 2020

Abstract We present an event of simultaneous observations of the northern and southern middle-altitude polar cusps by the Polar spacecraft and Cluster fleet that occurred on 23 September 2004. We examine the possible asymmetries in the fields and plasma parameters, although the proximity of the equinox should limit these asymmetries. Ion sensors reveal two dispersions in both cusps, and data analysis leads to the conclusion that those dispersions are due to pulsed reconnection at a single X-line, which runs along the subsolar magnetopause. While the electromagnetic and particle energy fluxes injected in both cusp are globally very similar, we report significant differences in ion dispersions, width of the low-latitude boundary layer, and peak convection velocities. We ascribe these differences to the dipole tilt that introduces an asymmetry in the magnetosheath flow at the exterior cusps.

1. Introduction

1.1. Polar Cusps

The polar cusps are the magnetospheric regions through which the shocked solar wind plasma has direct access to the magnetosphere and ionosphere. Those two funnel-shaped regions are small in the magnetosphere and so are their ionospheric footprints, but they play an important role in the plasma, energy, and momentum transfer from the solar wind to the magnetosphere and ultimately down to the upper polar atmosphere. Apart from being one of the densest regions of the magnetosphere, bringing in low-energy particles from the solar wind, they are also one of the most dynamic. The location of the polar cups is indeed very sensitive to the external conditions: solar wind dynamic pressure and interplanetary magnetic field (IMF) intensity and orientation (e.g., Newell et al., 1989; Pitout et al., 2006). Another feature commonly observed in the middle- or low-altitude cusps is the multiple ion dispersions or ion steps. Their origin has been ascribed to the acceleration process in the reconnection region (Newell & Meng, 1991), the temporal changing nature of the reconnection process (Escoubet et al., 1992; Lockwood & Smith, 1992, 1994), or the presence of several reconnection lines at the magnetopause (Trattner et al., 2005; Wing et al., 2001). While their dynamics and properties are overall well understood in a statistical sense, potential asymmetries between the two cusps have seldom been studied for obvious observational reasons: The Southern Hemisphere has been poorly explored, and having two spacecraft simultaneously in the two magnetospheric cusps is rare.

1.2. Hemispheric Asymmetries

It is well known that the high-latitude ionosphere and magnetosphere exhibit, at times, hemispheric asymmetries in their plasma and/or field properties.

Some of the causes of these asymmetries are obvious: The inclination of the Earth's axis of rotation induces a difference in insulation and therefore drives asymmetries in the ionospheric conductivities. Consequently, variations of the ground magnetic field are more pronounced in the sunlit hemisphere (Wescott, 1962). Also, this seasonal effect combined with the inclination of the magnetic axis (dipole tilt) results in asymmetries in the solar wind-magnetosphere-ionosphere coupled system. These are seen in the cusp location: Burch (1972) showed that the cusp lies at higher/lower latitude when the dipole tilts sunward/antisunward. This effect was quantified by Newell and Meng (1989). The role of the dipole tilt also shows up in ionospheric

convection patterns inferred from SuperDARN data: Pettigrew et al. (2010) reported clear statistical differences in the shape of the convection cells and in the cross-polar potential in the two hemispheres and explained these differences by the effect of the dipole tilt.

The auroral display may also exhibit strong differences in the two hemispheres. For instance, Stenbaek-Nielsen et al. (1973) noticed much brighter aurora in the Northern Hemisphere compared to the magnetically conjugate region. Using rare conjunctions of Polar and IMAGE spacecraft, Østgaard et al. (2005) or Laundal and Østgaard (2009) showed significant auroral asymmetries that were highly unexpected and challenged the current understanding of the mapping of the magnetic field between hemispheres and the acceleration processes that result in auroral emissions.

Newell and Meng (1988) showed another consequence of the seasonal effect: They performed a statistical study of DMSP F7 passes through the cusp and observed a strong asymmetry in low-energy precipitation near solstices. The authors ascribed this asymmetry to the faster magnetosheath flow above the winter hemisphere exterior cusp, preventing the low-energy particle to enter.

However, other—internal or external—sources of asymmetries may exist and lead to an asymmetric magnetosphere or ionosphere, even around equinoxes. For instance, the stronger magnetic field in the Southern Hemisphere (Laundal & Richmond, 2017) may account for some of the asymmetries observed in the populations of the two lobes (Haaland et al., 2017). Likewise, using the AMPERE experiment (Anderson et al., 2014), Coxon et al. (2016) noticed that around equinox, the Birkeland (field-aligned) currents flowing in the Northern Hemisphere are stronger than those flowing in the Southern Hemisphere. They explained this by different magnetic field and total electron content in the two hemispheres.

Among external sources, the magnetic reconnection process may also introduce north/south asymmetries in the magnetospheric system. It is clearly the case when the IMF points northward: Magnetic reconnection may then take place in one hemisphere but not in the other (e.g., Fuselier et al., 2014). This depends on the season (Wilder et al., 2013) but possibly equivalently on the orientation of the IMF in the (x_{GSM}, z_{GSM}) plane (effect of the cone angle). More unexpectedly, Berchem et al. (2016) have shown that the y-component of the IMF could also yield hemispheric asymmetries, at least under northward IMF.

1.3. Instrumentation

In this work, we analyze data from ESA's Cluster fleet (Escoubet et al., 2001) and NASA's Polar satellite (Harten & Clark, 1995). To monitor the entry of magnetosheath plasma into the magnetosphere and identify the polar cusp in the two hemispheres, we have used particle data from the CIS ion sensor (Rème et al., 2001) and PEACE electron sensor (Johnstone et al., 1997) on board Cluster and the HYDRA particle sensor (Scudder et al., 1995) on board Polar. Additionally, we estimate the Poynting flux and convection velocity using electric and magnetic fields measured by the electric field and wave (EFW, Gustafsson et al., 2001) and flux gate magnetometer (FGM, Balogh et al., 2001) experiments on board Cluster and the electric field instrument (EFI, Harvey et al., 1995) and magnetic field experiment (MFE, Russell et al., 1995) on board Polar. The external conditions are provided by the Geotail spacecraft: The MGF magnetometer (Kokubun et al., 1994) measures the IMF, and the solar wind properties are provided by the Comprehensive Plasma Instrument (CPI) described by Frank et al. (1994). SuperDARN (Greenwald et al., 1995) data complement the diagnostic by determining the time lag to apply between Geotail in the solar wind and Cluster and Polar in the cusps.

2. Observations on 23 September 2004

2.1. Orbital Configuration and External Conditions

On 23 September 2004, the northern and southern dayside magnetosphere are crossed near the noon sector at about the same time (~15:15 UT) by Polar in the Southern Hemisphere and the Cluster fleet in the Northern Hemisphere. Figure 1 displays two views of the spacecraft location in the $(y, z)_{GSM}$ and $(x, z)_{GSM}$ planes; some magnetic field lines given by the T96 model (Tsyganenko, 1995) are also displayed. The Cluster spacecraft were on a string of pearl configuration, following one another, with a separation of about 890 km between C1 and C4, the two satellites we shall focus on. This conjunction was found with the Conjunction Search Tool added to the 3DView on line service (Génot et al., 2018). At 15:20 UT, Cluster was located at (2.5, −0.4, 4.1) Earth's radii (R_E) in Geocentric Solar Magnetic coordinate system (GSM)

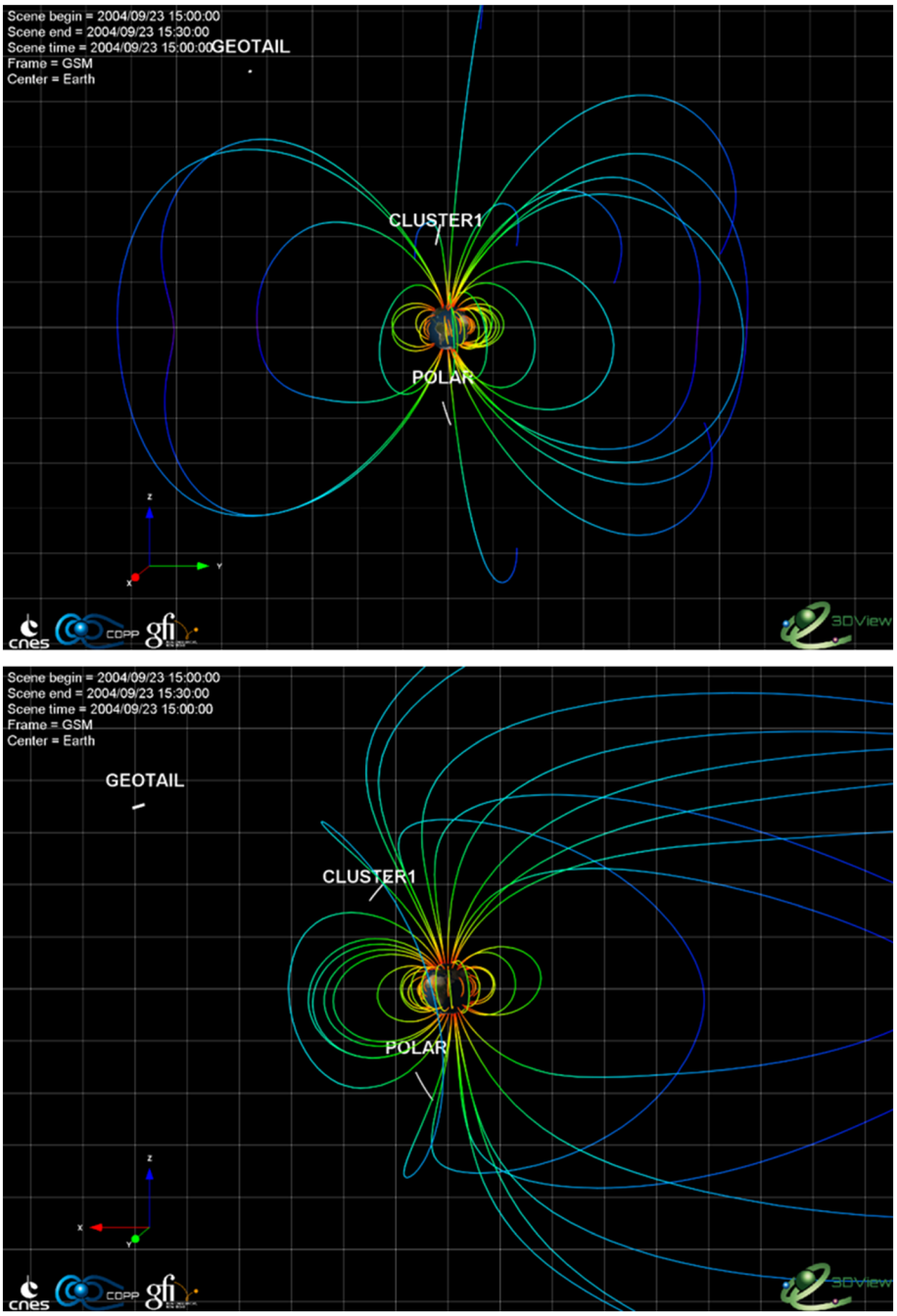

Figure 1. Cluster and Polar locations between 15::00 and 15:30 UTC on 23 September 2004 projected in the $(y, z)_{GSM}$ and $(x, z)_{GSM}$ planes (top and bottom, respectively). Superimposed to the figures are magnetospheric field lines from the Tsyganenko 96 model.

and Polar at (0.8, 0.0, −4.0) R_E GSM. These locations give geocentric distances of 4.8 R_E for Cluster and 4.0 R_E for Polar. The directions of motion of Cluster and Polar are both poleward, that is, northward for Cluster and southward for Polar. All spacecraft are located close to the magnetic noon, on the late morning side (Figure 1, top panel). Although close to equinox, a small asymmetry is visible in the northern and southern cusps in GSM: The grids in both panels of Figure 1 divide the planes in 1-Re^2 squares. The exterior cusp is located around (+2.5, +2) R_E in the Northern Hemisphere and (+1.5, −2.5) R_E in the southern so the northern cusp is more directed toward the Sun than the southern cusp (Figure 1, bottom

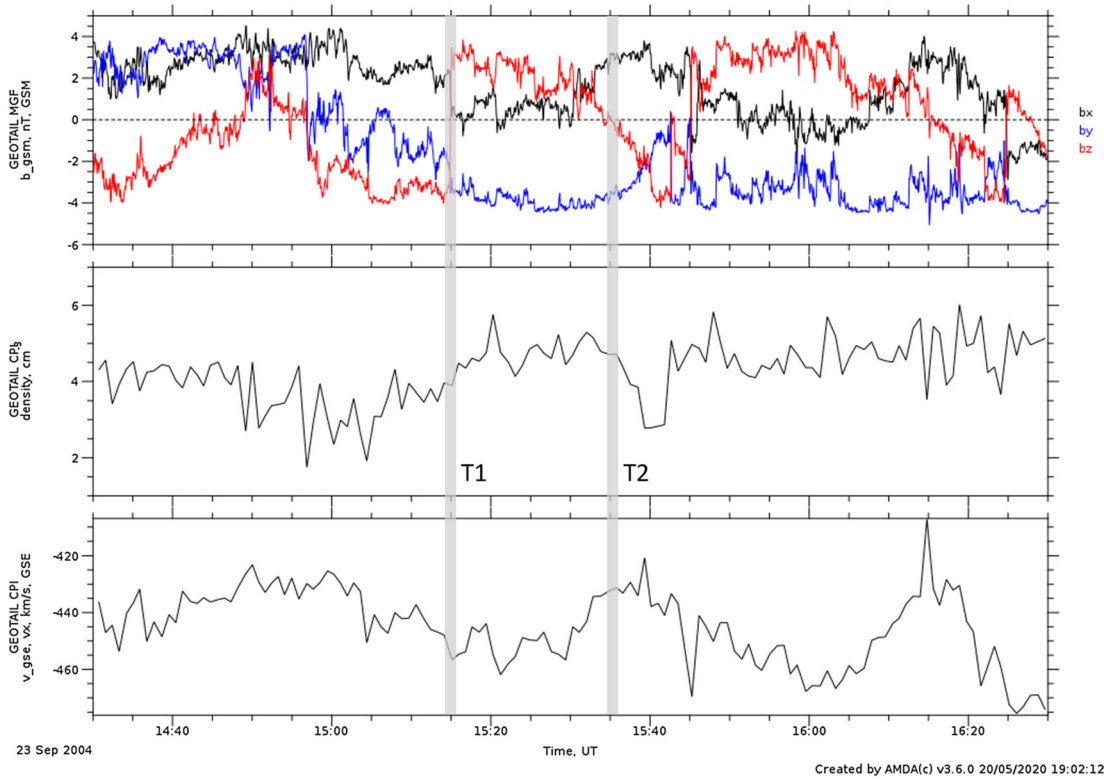

Figure 2. Three GSM components of the IMF (top panel), solar wind proton density, and X component of the solar wind velocity (middle and bottom panels) versus time at Geotail. The gray verticals tagged T1 and T2 correspond to the two IMF turnings discussed.

panel). The position of Cluster, having a larger X_{GSM} position than Polar when it flies through the cusp, also reflects this asymmetry.

External conditions (Figure 2) are given by the Geotail spacecraft, which was located just outside the bow shock at (13.5, −6, 8) R_E in the GSM coordinate system (Figure 1). During our time of interest, between 15:00 and 15:30 UT, the solar wind conditions remain relatively steady with a proton density around 4 cm^{-3} and an x component of the solar wind velocity around 450 km/s. The IMF is steady southward until 15:15 UT when the z component jumps from about −3 to +3 nT.

The timing of the IMF changes and their subsequent responses in the magnetosphere is an important matter in this study. To have a view as precise as possible, we have used SuperDARN radar data to monitor changes in the cusp location in response to IMF rotations. We have compared the IMF to data taken along Beam 7 of the Saskatoon radar, which covers well the area where the magnetic foot points of the Cluster spacecraft are (Figure 3). Figure 4 shows the data taken along Beam 7. The regions of backscattered signal are characterized by a strong away velocity (i.e., poleward velocity) of about 1 km/s (top panel of Figure 4), a high spectral width exceeding 200 m/s (middle panel), and a higher power (bottom panel). All these signatures are typical for the ionospheric cusp (Baker et al., 1990, 1995). The latitudinal motion of the cusp in response to the changes in the IMF helps us to determine the time delay between Geotail measurements and the cusp response. We know from numerous studies (e.g., Newell et al., 1989; Pitout et al., 2006) that for southward IMF conditions the cusp is located at lower latitudes while moving to higher latitudes during northward IMF conditions.

In Figure 4, abrupt changes in the cusp location are indicative of an IMF rotation. For instance, the northward turning of the IMF at 15:15 UT at Geotail (named T1 in Figure 2) triggers a poleward motion of the cusp starting at 15:30 UT (M1 in Figure 4). Likewise, the discontinuity seen in the cusp latitude around 15:50 UT (M2 in Figure 4) matches well the southward turning of 15:35 UT that reaches a minimum in B_z of −4 nT at 15:40 UT (T2 in Figure 2), thus a time lag of 10 to 15 min. This is consistent with the typical propagation time from the bow shock to the Earth's ionosphere of 10–16 min reported by Samsonov et al. (2018). Moreover, the magnetosphere as well as the ionospheric convection need about 4–6 min to adjust to the prevailing IMF

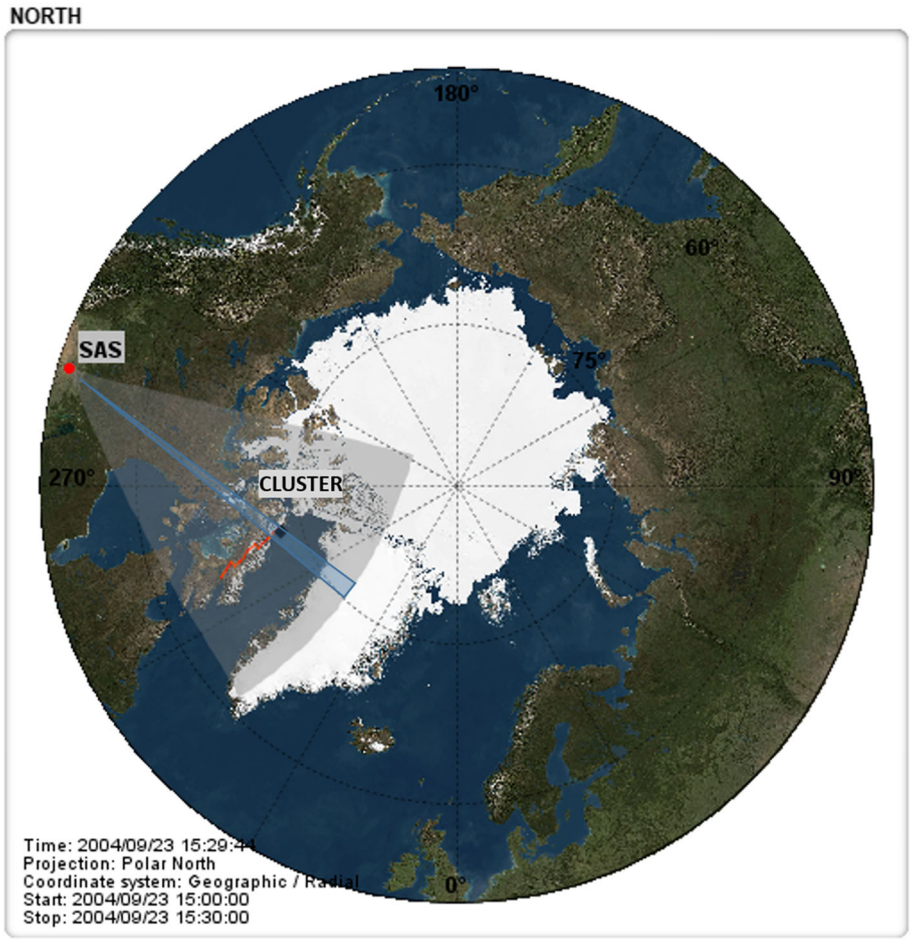

Figure 3. Polar view of Cluster 1 magnetic footprints (in orange) in the Northern Hemisphere. The field of view of the SuperDARN Saskatoon radar is shown in gray, as well as its Beam 7 in blue.

conditions (Pitout et al., 2001; Taylor et al., 1998; Trattner et al., 2016) so a time lag between observations at Geotail and in the magnetospheric cusps is probably closer to 10 min. We shall adopt this value from now on.

Let us emphasize that this event was already studied from the point of view of Cluster (Escoubet et al., 2008), and we shall occasionally refer to that study. In that paper, the authors studied the consequences of the IMF rotation that occurs at 15:15 UT at Geotail.

2.2. Location and Morphological Features of the Cusps

Figure 5 shows the lagged IMF measured by MGF on board Geotail and three ion *spectrograms* of the differential energy flux (for 0–15° pitch angle) from Cluster 1 CIS-HIA, Cluster 4 CIS-CODIF, and Polar HYDRA. The three spectrograms are recorded, while the prevailing IMF is southward. The signature of the polar cusp in ion spectrograms usually exhibits a typical energy-time dispersion. This feature is clearly seen in data from all three spacecraft. The orientation of those dispersions, with decreasing energies observed with increasing latitude, is consistent with the IMF pointing southward (e.g., Pitout et al., 2009; Reiff et al., 1977). One can also notice that two dispersions are clearly seen in the data from all spacecraft.

Figure 6 displays electron and ion spectrograms measured by the HYDRA instrument on board Polar (two top panels) and electron and ion spectrograms from the CIS-HIA and PEACE instruments respectively on board Cluster (two bottom panels) as a function of the AACGM magnetic latitude (Shepherd, 2014). It is interesting to compare the locations of the open-closed field line boundaries (OCB) and the cusp equatorward boundaries (CEB). Assuming high fluxes of keV electrons are on closed field lines and ~100 eV on open field lines, we can locate the OCB around 77.2° AACGM latitude in the south and 77.8° in the north. Likewise, the CEB, defined where the first ~keV dispersed ions are observed, is seen at a somewhat lower AACGM latitude in the

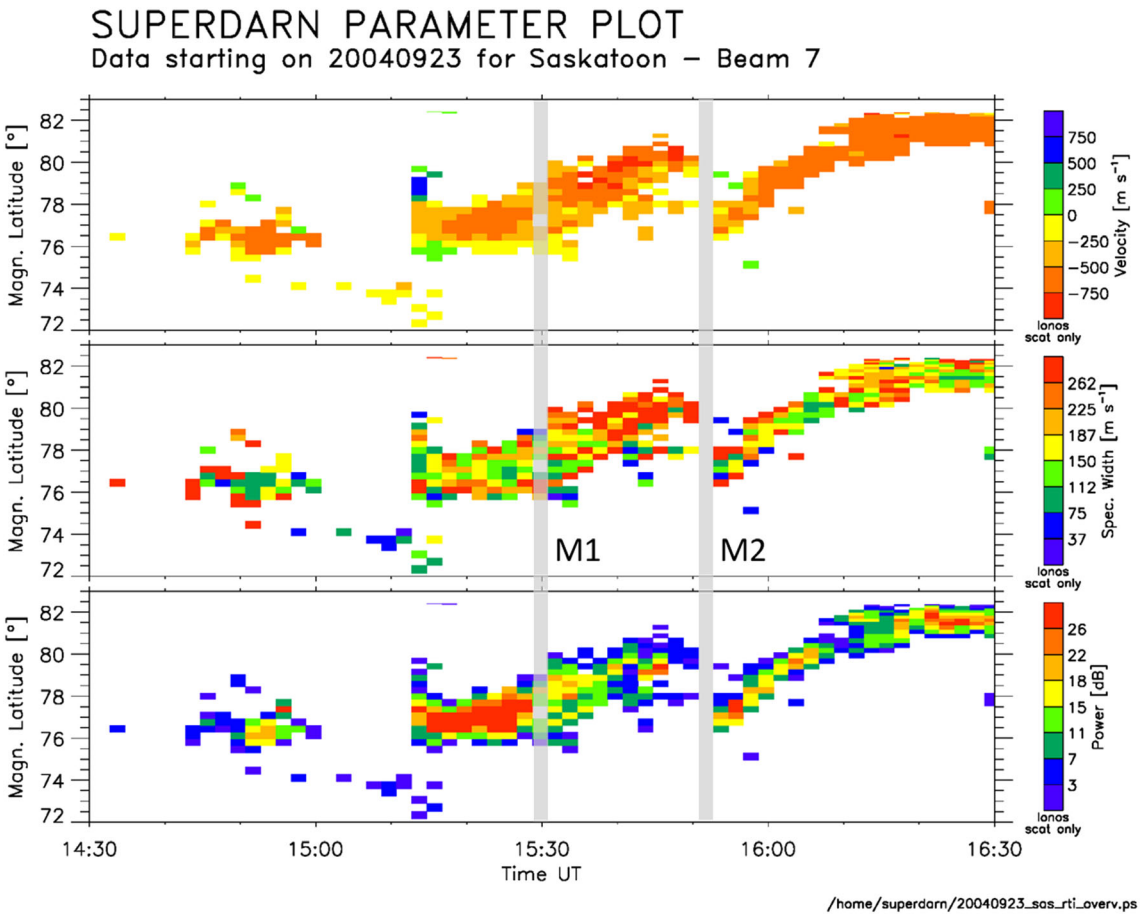

Figure 4. SuperDARN data taken by the Saskatoon radar between 14:30 and 16:30 UT on 23 September 2004. The three color panels show, from top to bottom, the line-of-sight plasma velocity in m/s, the spectral width in m/s, and the backscattered power in dB measured along Beam 7. The two gray vertical lines mark the cusp motion in response to two rotations of the IMF.

south: 77.7° versus 78.0° in the north. The OCB and CEB are shown as magenta and white vertical lines in Figure 6. Consequently, the width of the electron boundary layer (between the first detected low-energy electrons and ions) is wider at Polar in the Southern Hemisphere (~0.5°) than at Cluster in the Northern Hemisphere (~0.2°). In principle, this is indicative of a faster plasma sheath flow in the Southern Hemisphere, where Polar is located (Newell & Meng, 1987). We should note that these boundaries may be moving back and forth with respect to the spacecraft since we can observe short interruptions of energetic electrons (above 1,000 keV) on Cluster (2) and Polar (1). The second dispersion on Cluster is not as clear as in Figure 4 since omnidirectional flux is plotted and particles going downward and upward are mixed.

2.3. Particle Density in the Cusps

Near equinox and irrespective of the tilt angle, one can expect a symmetric filling of the two cusps and therefore identical plasma properties. The ion densities given by CIS on board Cluster 1 and Cluster, and by HYDRA on board Polar are shown in Figure 7. Their values are quite comparable, around 6–8 cm^{-3}, slightly lower at Polar in the Southern Hemisphere cusp, but this difference might not be significant.

3. Interpretation and Discussion

3.1. Consequence on the Pulsating Nature of Reconnection

The ion dispersions observed at Cluster and Polar have the two properties that have strong implications regarding the reconnection process at play.

On each spectrogram, the successive ion dispersions do not overlap each other. This indicates we are not in presence of a multiple X-line (Fu & Lee, 1985; Lee & Fu, 1985, 1986) but rather of temporal structures due to

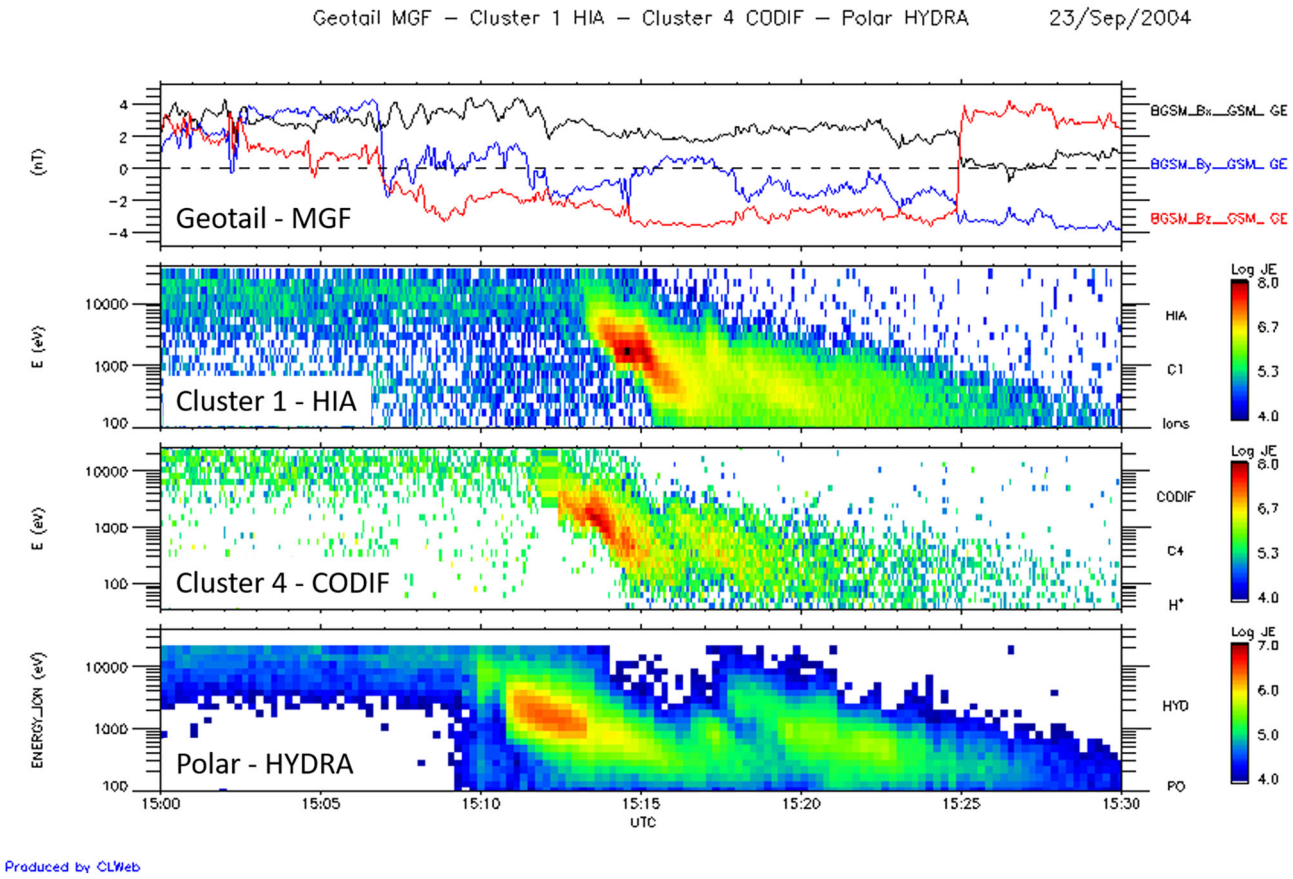

Figure 5. Composite plot with, from top to bottom: the interplanetary magnetic field measured by MGF on board Geotail (the data are time shifted by 10 min), differential energy flux of ions given by Cluster 1-HIA, Cluster 4-CODIF (H + only), and Polar-HYDRA.

pulsed reconnection (Boudouridis et al., 2001; Lockwood & Davis, 1995; Lockwood et al., 1993). To the authors' knowledge, it is the first time that the consequence of pulsed reconnection is observed simultaneously in the two polar cusps.

The first dispersions end and second ones start at about the same time. This is consistent with satellites being at about the same distance to the reconnection site. Given their location and altitude, this means that the reconnection site should be close to the magnetic equator. The maximum shear model (Trattner et al., 2007) around 15:19 UT (Figure 8) predicts a reconnection line running along the dayside magnetopause very close to the subsolar point. This point will be verified in the next subsection.

3.2. Distance to and Location of the Reconnection Site

We use here the time of flight effect (Rosenbauer et al., 1975) applied to the lower cutoff energy of the cusp ions (Lockwood, 1997; Lockwood & Smith, 1994) to estimate the distance along the magnetic field lines between the satellite, where cusp particles are detected, and the reconnection site, where the same cusp particles are injected. The energy E_i of a given zero pitch angle ion of mass m as a function of the distance to the reconnection site d and the time of flight $t_i - t_0$ is given by Lockwood and Davis (1995) and Lockwood (1997):

$$E_i = \frac{m}{2}\frac{d^2}{(t_i - t_0)^2}$$

This yields the distance to the reconnection:

$$d = \frac{(t_2 - t_1)}{\frac{1}{V_2} - \frac{1}{V_1}}$$

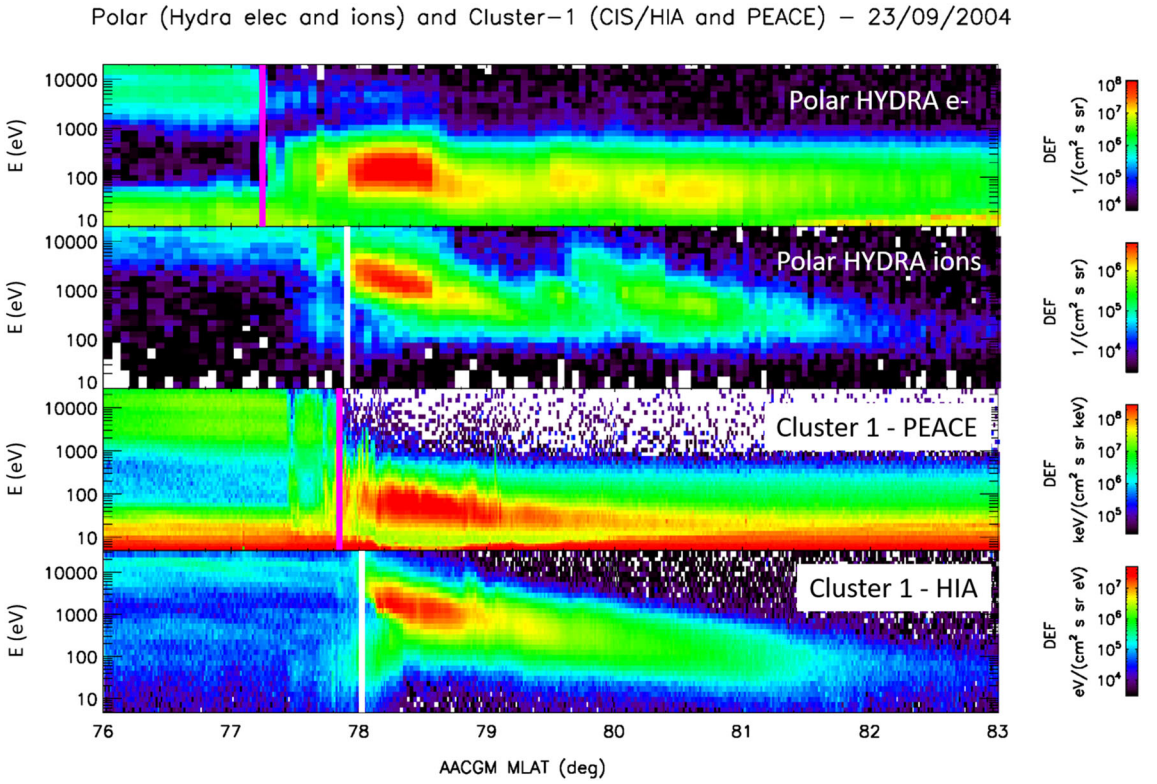

Figure 6. Electron and ion differential energy flux spectra as a function of AACGM latitude from Polar (top panels) and Cluster 1 (bottom panels). OCB are shown in magenta and CEB in white.

where V_1 and V_2 are the ion velocities of the lowest-energy and zero pitch angle ions measured at times t_1 and t_2. After plotting the ion dispersion in a $1/V$-time spectrogram (where V is the velocity of precipitating ions), the slope of the dispersion gives us directly an estimate of the distance to the reconnection site along the local magnetic field line. In practice, (t_1, V_1) and (t_2, V_2) are taken along a line of constant energy flux. Depending of the values chosen, the distance obtained may vary slightly.

At Cluster, we obtain values between 9.4 and 11.6 R_E depending on the reference points one takes. These values are in good agreement with Escoubet et al. (2008) who found 11.4 R_E with another technique.

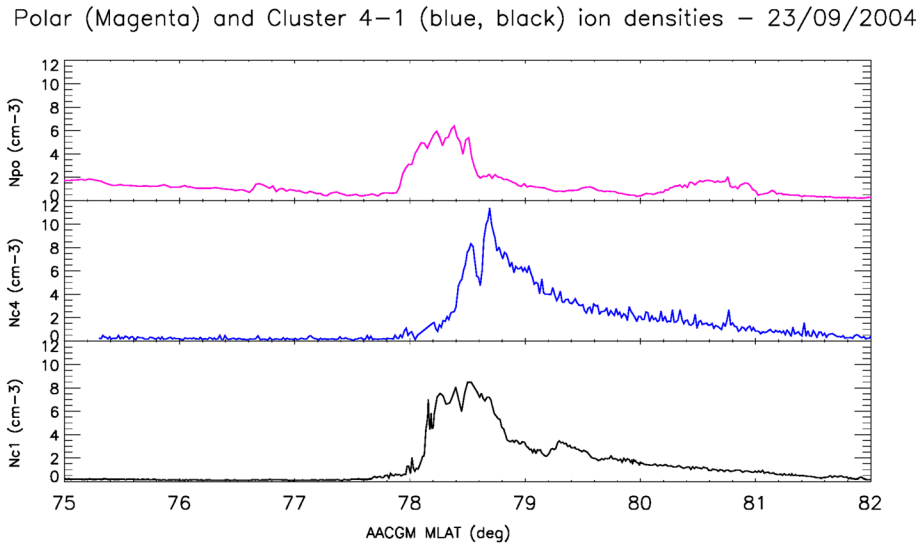

Figure 7. Ion densities measured on board Polar (top panel) and Cluster 4 and Cluster 1 (middle and bottom panels).

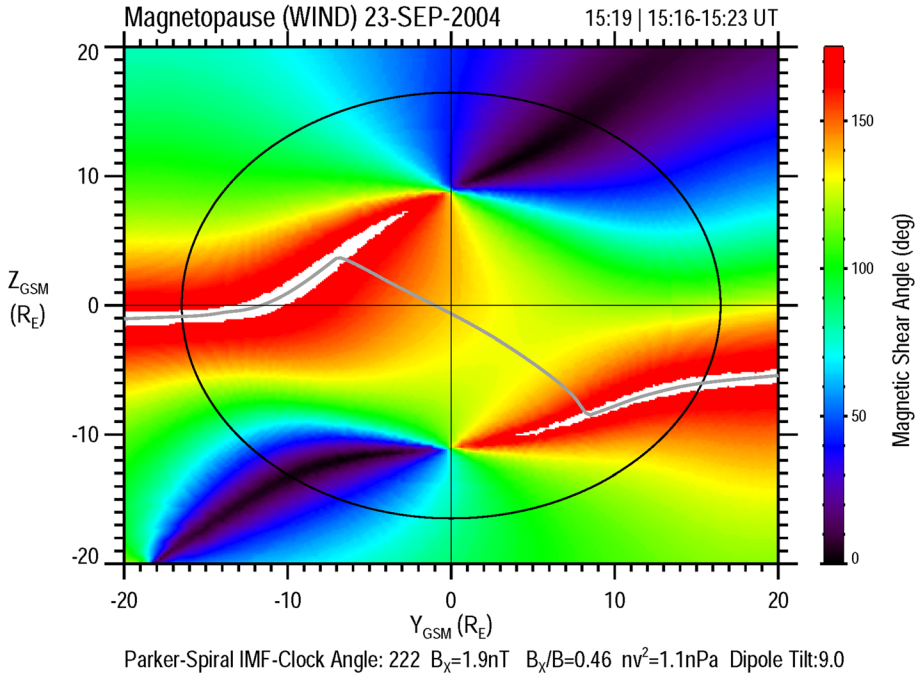

Figure 8. Magnetic shear angle at Earth between the IMF and the geomagnetic field. The gray line corresponds to the expected reconnection line according to the maximum shear model. The intersection between the magnetopause and the (X_{GSM}, Z_{GSM}) plane is depicted in black.

Given the altitude of the spacecraft—or rather its distance to the ground level along the local magnetic field line—this is equivalent to a distance along the field line from the surface of the Earth to the reconnection point between 13.2 and 15.4 R_E.

At Polar, we find a distance to the reconnection site of the order of 11–12.5 R_E, which means a distance between the reconnection point and the surface of the Earth between 14 and 15.5 R_E.

For comparison, the Tsyganenko 02 (T02) model (Tsyganenko, 2002a, 2002b) gives a length, from surface to surface in the two opposite hemispheres, of the last closed magnetic field line of 32.7 R_E. This value is close to the addition of the two values found from the ion dispersions (around 30 R_E). All this suggests that the reconnection line is located very close to or at the subsolar magnetopause and that both Cluster and Polar ion dispersions come from the same reconnection line.

3.3. Energy Input

To estimate the electromagnetic energy injected into the two cusps, the magnetic and electric fields measured at both spacecraft were used to calculate the Poynting flux (Kelley et al., 1991). The Poynting vector $\vec{S}$ is defined as follows:

$$\vec{S} = \frac{\vec{E} \times \delta\vec{B}}{\mu_0}$$

where $\vec{E}$ is the measured electric field, $\delta\vec{B}$ the magnetic field variation (we have removed the background field by fitting the total measured field before and after the cusp crossings), and μ_0 is the vacuum permeability.

S_B, the component of $\vec{S}$ parallel to $\vec{B}$, determined at Cluster 1 and Polar is given in Figures 9a and 9c. The power is globally injected toward the Earth in both cases: positive values at Cluster in the Northern Hemisphere and negative values in the Southern Hemisphere at Polar. Peak values reach about 0.2 mW/m^2 in both hemispheres.

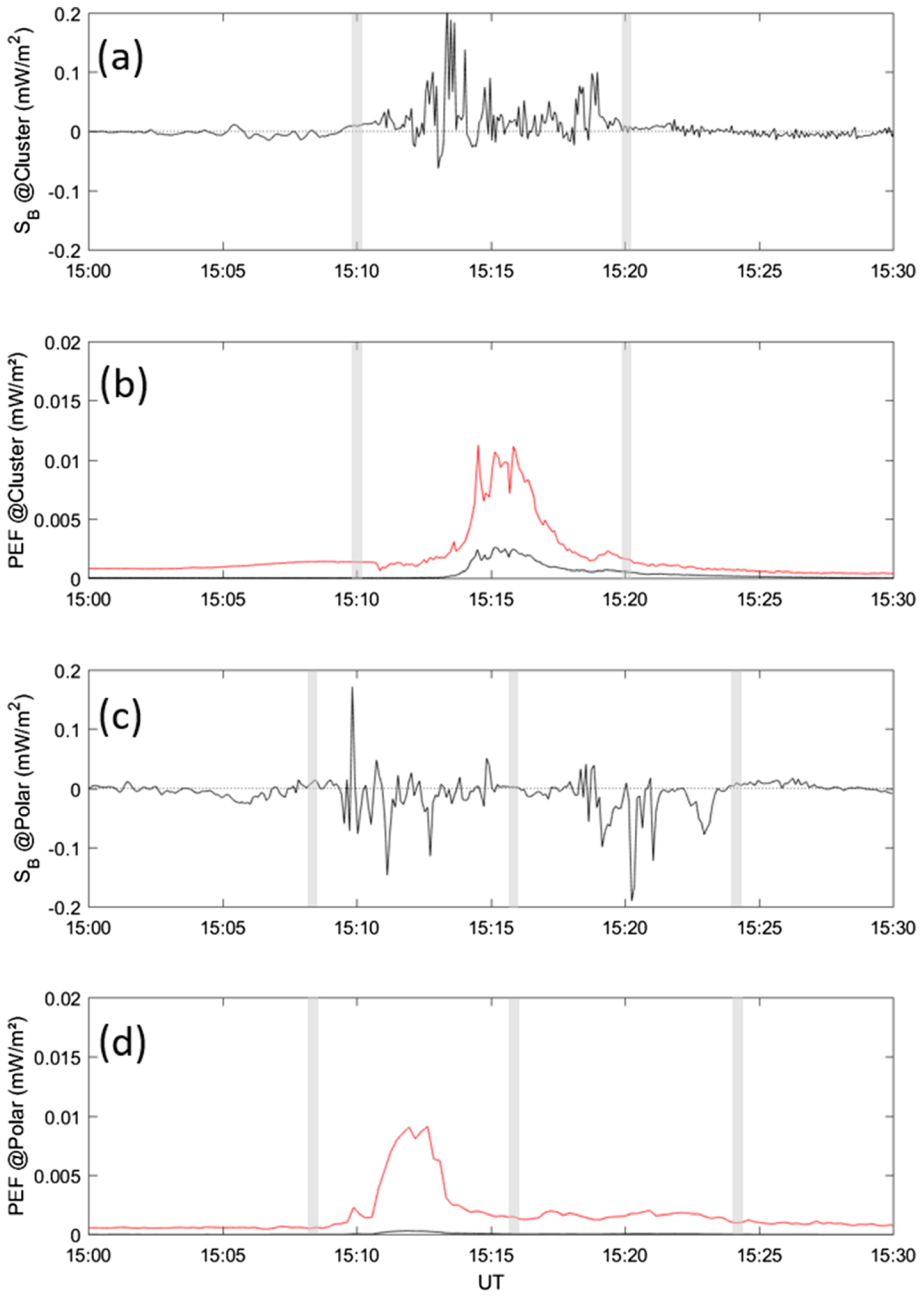

Figure 9. Panels (a) and (c) show for Cluster 1 the field-aligned Poynting flux and Cluster 1 and Polar; panels (b) and (d) display the total particle energy flux (PEF) carried by electrons (red) and ions (black) at Polar. The gray vertical bars indicate the boundaries taken for the integrations.

Knowing that the velocity of the two spacecraft is about 4.5 km/s and that the time interval considered lasts 600 s at Cluster 1 (from 15:10 to 15:20 UT) and 960 s at Polar (from 15:08 to 15:24 UT), we may integrate over the latitudinal width of the cusp. We obtain +59.4 W/m at Cluster and −60.5 W/m at Polar. (The plus sign in the Northern Hemisphere and the minus in the Southern Hemisphere both mean that the power is injected toward the Earth.) We find very similar values for both hemispheres; the energy injected from the solar wind into the magnetosphere is thus equally distributed through the two cusps.

It is interesting to note that the total amount of energy at Polar remarkably equals that measured at Cluster only if one considers the two dispersions recorded at each spacecraft. If not, the first dispersion recorded at

Polar injects little energy (−20 W/m) compared to the second one (−40 W/m), while at Cluster, the first dispersion contains +40 W/m and the second +20 W/m.

The latter result is surprising because the particle energy fluxes show the opposite trend: The energy flux in the first dispersions is higher than in the second ones. Figures 9b and 9c show the total energy fluxes carried by the electrons (red) and ions (black) at Cluster 1 and Polar. In both cusps, we find values of the order 0.01 mW/m^2 for the electrons, which carry most of the energy.

These results deserve some comments. The energy flux carried by the particles is about 10 times smaller than that transported by the Poynting flux; this is not uncommon (Korth et al., 2005). Then, the first dispersions correspond well with the downward Poynting fluxes. We have integrated over the whole cusp crossings as we did for the Poynting fluxes. This gives integrated energy fluxes of 11.9 W/m at Cluster in the northern cusp (9.7 W/m carried by electrons and 2.2 by ions). At Polar, in the southern cusp, we obtain 10.9 W/m (10.6 W/m carried by electrons and 0.3 W/m by ions). We confirm once again that the particles in the cusp contain similar energy in both cusp. It has to be noted that the ion energy flux in the southern cusp measured by Polar is significantly lower than that measured by Cluster. Although this has very little effect on the total particle energy flux, this could be explained by the different energy range of the HIA and HYDRA sensors or their different evolution in time. The second dispersion at Polar contains only 3.5 W/m of integrated particle flux (about one third of the 10.9 W/m), while according to the electric and magnetic field instruments, 40 W/m (two thirds of the 60.5 W/m) is injected toward the Earth. Such a mismatch is difficult to interpret. This kind of decorrelation has already been observed in 25% of the cases studied by Deng et al. (2015) and interpreted as a reconfiguration of the magnetosphere-ionosphere system following a change in the IMF. In our case, smaller changes in the x and z components of the IMF are recorded at Geotail between 15:20 and 15:35 UT but it remains unclear whether they might cause our observations.

Another way of comparing the energy input in the magnetosphere is in principle to look at the cross-polar cap electric potential. Estimates provided by the SuperDARN network between 15:14 and 15:16 UT for instance are 51 and 52 kV for the Northern and Southern Hemispheres, respectively. A word of caution though: While the values for the Northern Hemisphere can be trusted (the radar coverage is good), the values for the Southern Hemisphere have to be handled with much care due to a poor radar coverage.

3.4. Convection Velocity and Magnetosheath Flow

Having the electric field $\vec{E}$ and the magnetic field $\vec{B}$, it is straightforward to obtain the convection velocity at each satellite:

$$\vec{V} = \frac{\vec{E} \times \vec{B}}{B^2}$$

Figure 10 shows the convection velocities calculated at Cluster 1 and Polar. The average convection velocity in the cusp is about 9.0 km/s at Polar and 9.8 km/s at Cluster. We may consider the different altitudes of Cluster and Polar and adjust the velocity found at Polar to the altitude of Cluster. To do so, we assume that there is no potential drop along a given field line and we apply a scaling factor on the convection velocity due to the change of magnitude of the magnetic field with the altitude. This scaling factor is obtained with the T02 model (Tsyganenko, 2002a, 2002b). We find an average velocity of 9.9 km/s. The average convection velocities are essentially the same in both hemisphere. However, peak velocities measured at Polar reach at best 20 km/s while they often exceed 40 km/s at Cluster. These differences cannot be explained by the altitude difference only, neither by the different shapes of the ion dispersions. Of course, one has to bear in mind that these differences may also come from the two electric field instruments, which have different designs (additional container for the bias current electronics at the end of wire boom included on Cluster).

The dipole tilt in the $(x, z)_{GSM}$ plane during this event is about +9°. While this value is small, it is large enough to yield the exterior northern cusp at a larger X_{GSM} and lower Z_{GSM} (in absolute value) than the southern cusp. In other words, the northern cusp is located at lower magnetic latitude than the southern one. This implies a faster magnetosheath flow at the southern exterior cusp (Spreiter et al., 1966).

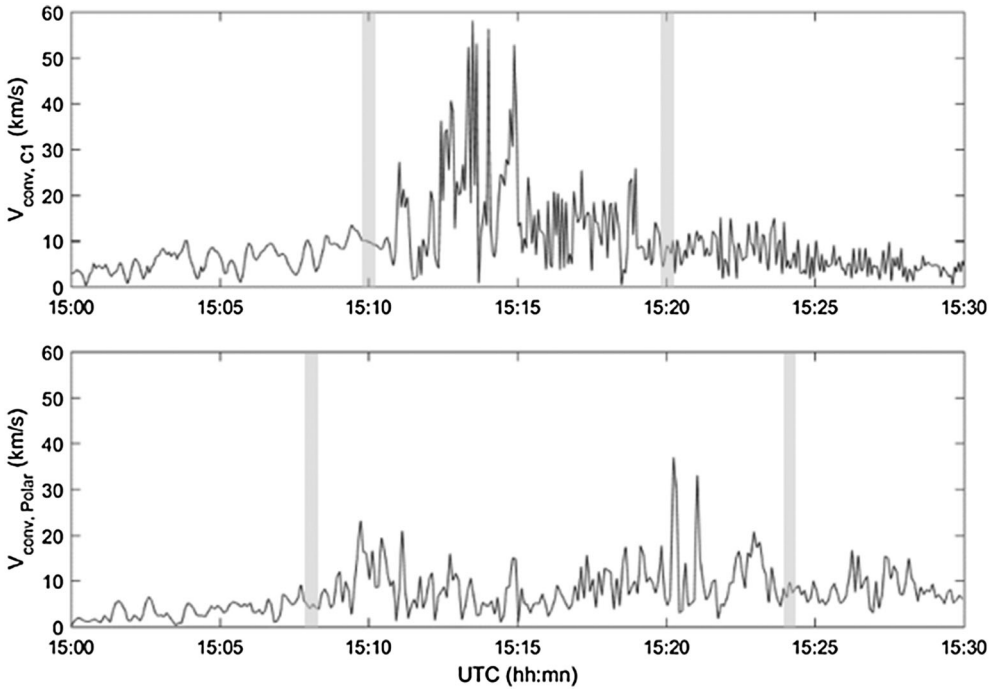

Figure 10. Convection velocities measured at Cluster 1 (top panel) and Polar (bottom panel). The gray vertical bars indicate the boundaries taken for the averaging.

4. Summary

We have reported on an event of simultaneous in situ observations of the northern and southern polar cusps by Polar and Cluster on 23 September 2004. This event is interesting for two reasons: (i) simultaneous cusp crossing are quite rare and (ii) this one occurred only 2 days after the Autumn equinox, which should in principle limit hemispherical asymmetries of seasonal (geometric) origin.

In many respects, the two cusps crossings presented in this paper look indeed the same: Both spacecraft observe two ion dispersions, which seem to be the signature of pulsed reconnection in the cusp; they record similar ion density, average convection velocity, and energy input (Poynting flux and particle energy flux).

From this specific event, we can confirm that near equinox, dayside electromagnetic and particle energy transfer from the solar wind to the magnetosphere is indeed evenly distributed between the two cusps. However, peak convection velocities and ion dispersions exhibit substantial differences that may be the consequences of the (weak) tilt angle, implying that the two cusps find themselves at slightly different magnetic latitudes. More of those simultaneous cusp crossings should be studied—and modeled—to confirm this hypothesis. In addition, a mismatch between the distribution of Poynting flux and particle energy flux has been found at Polar and remains unexplained.

Data Availability Statement

OMNI data (solar wind and IMF parameters) were retrieved through the AMDA website (http://amda.cdpp.eu; they are also available at https://omniweb.gsfc.nasa.gov/). Cluster and Polar data have been plotted with CLWeb (http://clweb.irap.omp.eu/). SuperDARN data are available at Virginia Tech (http://vt.superdarn.org). Figures 1 and 3 showing the (projected) orbits of Cluster and Polar were generated by 3DView (http://3dview.cdpp.eu). Simulation results have been provided by the Community Coordinated Modeling Center at Goddard Space Flight Center through their public Runs on Request system (http://ccmc.gsfc.nasa.gov).

Acknowledgments

The 3DView and the Conjunction Search Tool were funded by CNES. The T96 and T02 models were developed by N. Tsyganenko at the University of St. Petersburg, Russia. This work was supported by the Programme National PNST of CNRS/INSU cofunded by CNES and Commissariat à l'Énergie Atomique et aux Énergies Alternatives (CEA). The work at UCLA was supported by NASA Grant No. 80NSSC19K0846. We would like to thank Emmanuel Penou and Iannis Dandouras of IRAP for their assistance.

References

Anderson, B. J., Korth, H., Waters, C. L., Green, D. L., Merkin, V. G., Barnes, R. J., & Dyrud, L. P. (2014). Development of large-scale Birkeland currents determined from the active magnetosphere and planetary electrodynamics response experiment. *Geophysical Research Letters*, *41*, 3017–3025. https://doi.org/10.1002/2014GL059941

Baker, K. B., Dudeney, J. R., Greenwald, R. A., Pinnock, M., Newell, P. T., Rodger, A. S., et al. (1995). HF radar signatures of the cusp and low-latitude boundary layer. *Journal of Geophysical Research*, *100*(A5), 7671. https://doi.org/10.1029/94JA01481

Baker, K. B., Greenwald, R. A., Ruohoniemi, J. M., Dudeney, J. R., Pinnock, M., Newell, P. T., et al. (1990). Simultaneous HF radar and DMSP observations of the cusp. *Geophysical Research Letters*, *17*(11), 1869–1872. https://doi.org/10.1029/GL017i011p01869

Balogh, A., Carr, C. M., Acuña, M. H., Dunlop, M. W., Beek, T. J., Brown, P., et al. (2001). The cluster magnetic field investigation: Overview of in-flight performance and initial results. *Annales de Geophysique*, *19*(10/12), 1207–1217. https://doi.org/10.5194/angeo-19-1207-2001

Berchem, J., Richard, R. L., Escoubet, C. P., Wing, S., & Pitout, F. (2016). Asymmetrical response of dayside ion precipitation to a large rotation of the IMF. *Journal of Geophysical Research: Space Physics*, *121*, 263–273. https://doi.org/10.1002/2015JA021969

Boudouridis, A., Spence, H. E., & Onsager, T. G. (2001). Investigation of magnetopause reconnection models using two colocated, low-altitude satellites: A unifying reconnection geometry. *Journal of Geophysical Research*, *106*(A12), 29,451–29,466. https://doi.org/10.1029/2000JA000350

Burch, J. L. (1972). Precipitation of low-energy electrons at high latitudes: Effects of interplanetary magnetic field and dipole tilt angle. *Journal of Geophysical Research*, *77*(34), 6696–6707. https://doi.org/10.1029/JA077i034p06696

Coxon, J. C., Milan, S. E., Carter, J. A., Clausen, L. B. N., Anderson, B. J., & Korth, H. (2016). Seasonal and diurnal variations in AMPERE observations of the Birkeland currents compared to modeled results. *Journal of Geophysical Research: Space Physics*, *121*, 4027–4040. https://doi.org/10.1002/2015JA022050

Deng, Y., Sheng, C., Su, Y.-J., Hairston, M. R., Knipp, D., Huang, C. Y., et al. (2015). Correlation between Poynting flux and soft precipitation in the dayside polar cap boundary regions. *Journal of Geophysical Research: Space Physics*, *120*, 9102–9109. https://doi.org/10.1002/2015JA021075

Escoubet, C. P., Berchem, J., Bosqued, J. M., Trattner, K. J., Taylor, M. G. G. T., Pitout, F., et al. (2008). Effect of a northward turning of the interplanetary magnetic field on cusp precipitation as observed by Cluster. *Journal of Geophysical Research*, *113*, A07S13. https://doi.org/10.1029/2007JA012771

Escoubet, C. P., Fehringer, M., & Goldstein, M. (2001). The Cluster mission. *Annales de Geophysique*, *19*(10/12), 1197–1200. https://doi.org/10.5194/angeo-19-1197-2001

Escoubet, C. P., Smith, M. F., Fung, S. F., Anderson, P. C., Hoffman, R. A., Basinska, E. M., & Bosqued, J. M. (1992). Staircase ion signature in the polar cusp—A case study. *Geophysical Research Letters*, *19*(17), 1735–1738. https://doi.org/10.1029/92GL01806

Frank, L. A., Ackerson, K. L., Paterson, W. R., Lee, J. A., English, M. R., & Pickett, G. L. (1994). The comprehensive plasma instrumentation (CPI) for the GEOTAIL spacecraft. *Journal of Geomagnetism and Geoelectricity*, *46*(1), 23–37. https://doi.org/10.5636/jgg.46.23

Fu, Z. F., & Lee, L. C. (1985). Simulation of multiple X-line reconnection at the dayside magnetopause. *Geophysical Research Letters*, *12*(5), 291–294. https://doi.org/10.1029/GL012i005p00291

Fuselier, S. A., Petrinec, S. M., Trattner, K. J., & Lavraud, B. (2014). Magnetic field topology for northward IMF reconnection: Ion observations. *Journal of Geophysical Research: Space Physics*, *119*, 9051–9071. https://doi.org/10.1002/2014JA020351

Génot, V., Beigbeder, L., Jacquey, C., Rouillard, A., Gangloff, M., Popescu, D., et al. (2018). Science data visualization in planetary and heliospheric contexts with 3DView. *Planetary and Space Science*, *150*, 111–130. https://doi.org/10.1016/j.pss.2017.07.007

Greenwald, R. A., Baker, K. B., Dudeney, J. R., Pinnock, M., Jones, T. B., Thomas, E. C., et al. (1995). DARN/SuperDARN: A global view of the dynamics of high-latitude convection. *Space Science Reviews*, *71*(1–4), 761–796. https://doi.org/10.1007/BF00751350

Gustafsson, G., André, M., Carozzi, T., Eriksson, A. I., Fälthammar, C. G., Grard, R., et al. (2001). First results of electric field and density observations by Cluster EFW based on initial months of operation. *Annales de Geophysique*, *19*(10/12), 1219–1240. https://doi.org/10.5194/angeo-19-1219-2001

Haaland, S., Lybekk, B., Maes, L., Laundal, K., Pedersen, A., Tenfjord, P., et al. (2017). North-south asymmetries in cold plasma density in the magnetotail lobes: Cluster observations. *Journal of Geophysical Research: Space Physics*, *122*, 136–149. https://doi.org/10.1002/2016JA023404

Harten, R., & Clark, K. (1995). The design features of the GGS Wind and Polar spacecraft. *Space Science Reviews*, *71*(1–4), 23–40. https://doi.org/10.1007/BF00751324

Harvey, P., Mozer, F. S., Pankow, D., Wygant, J., Maynard, N. C., Singer, H., et al. (1995). The electric field instrument on the polar satellite. *Space Science Reviews*, *71*(1–4), 583–596. https://doi.org/10.1007/BF00751342

Johnstone, A. D., Alsop, C., Burge, S., Carter, P. J., Coates, A. J., Coker, A. J., et al. (1997). Peace: A plasma electron and current experiment. *Space Science Reviews*, *79*(1/2), 351–398. https://doi.org/10.1023/A:1004938001388

Kelley, M. C., Knudsen, D. J., & Vickrey, J. F. (1991). Poynting flux measurements on a satellite: A diagnostic tool for space research. *Journal of Geophysical Research*, *96*(A1), 201–207. https://doi.org/10.1029/90JA01837

Kokubun, S., Yamamoto, T., Acuña, M. H., Hayashi, K., Shiokawa, K., & Kawano, H. (1994). The GEOTAIL magnetic field experiment. *Journal of Geomagnetism and Geoelectricity*, *46*(1), 7–21. https://doi.org/10.5636/jgg.46.7

Korth, H., Anderson, B. J., Frey, H. U., & Waters, C. L. (2005). High-latitude electromagnetic and particle energy flux during an event with sustained strongly northward IMF. *Annales de Geophysique*, *23*(4), 1295–1310. https://doi.org/10.5194/angeo-23-1295-2005

Laundal, K. M., & Østgaard, N. (2009). Asymmetric auroral intensities in the Earth's northern and southern hemispheres. *Nature*, *460*(7254), 491–493. https://doi.org/10.1038/nature08154

Laundal, K. M., & Richmond, A. D. (2017). Magnetic coordinate systems. *Space Science Reviews*, *206*, 27–59. https://doi.org/10.1007/s11214-016-0275-y

Lee, L. C., & Fu, Z. F. (1985). A theory of magnetic flux transfer at the Earth's magnetopause. *Geophysical Research Letters*, *12*(2), 105–108. https://doi.org/10.1029/GL012i002p00105

Lee, L. C., & Fu, Z. F. (1986). Multiple X line reconnection: 1. A criterion for the transition from a single X line to a multiple X line reconnection. *Journal of Geophysical Research*, *91*(A6), 6807. https://doi.org/10.1029/JA091iA06p06807

Lockwood, M. (1997). Energy and pitch-angle distribution of LLBL/cusp ions seen at middle altitudes predictions by open magnetosphere model. *Annales Geophysicae*, *15*(12), 1501–1514. https://doi.org/10.1007/s00585-997-1501-4

Lockwood, M., & Davis, C. J. (1995). Occurrence probability, width and number of steps of cusp precipitation for fully pulsed reconnection at the dayside magnetopause. *Journal of Geophysical Research*, *100*(A5), 7627–7640. https://doi.org/10.1029/94JA02197

Lockwood, M., Dening, W. F., Farmer, A. D., Davda, V. N., Cowley, S. W. H., & Lühr, H. (1993). Ionospheric signatures of pulsed reconnection at the Earth's magnetopause. *Nature*, *361*(6411), 424–428. https://doi.org/10.1038/361424a0

Lockwood, M., & Smith, M. F. (1992). The variation of reconnection rate at the dayside magnetopause and cusp ion precipitation. *Journal of Geophysical Research*, *97*(14), 841.

Lockwood, M., & Smith, M. F. (1994). Low and middle altitude cusp particle signatures for general magnetopause reconnection rate variations: 1. Theory. *Journal of Geophysical Research*, *99*(A5), 8531. https://doi.org/10.1029/93JA03399

Newell, P. T., & Meng, C.-I. (1987). Cusp width and B_z: Observations and a conceptual model. *Journal of Geophysical Research*, *92*(A12), 13,673–13,678. https://doi.org/10.1029/JA092iA12p13673

Newell, P. T., & Meng, C.-I. (1988). Hemispherical asymmetry in cusp precipitation near solstices. *Journal of Geophysical Research*, *93*(A4), 2643–2648. https://doi.org/10.1029/JA093iA04p02643

Newell, P. T., & Meng, C.-I. (1989). Dipole tilt angle effects on the latitude of the cusp and cleft/low-latitude boundary layer. *Journal of Geophysical Research*, *94*(A6), 6949–6953. https://doi.org/10.1029/JA094iA06p06949

Newell, P. T., & Meng, C.-I. (1991). Ion acceleration at the equatorward edge of the cusp: Low-altitude observations of patchy merging. *Geophysical Research Letters*, *18*(10), 1829–1832. https://doi.org/10.1029/91GL02088

Newell, P. T., Meng, C.-I., Sibeck, D., & Lepping, R. (1989). Some low-altitude cusp dependencies on the interplanetary magnetic field. *Journal of Geophysical Research*, *94*(A7), 8921. https://doi.org/10.1029/JA094iA07p08921

Østgaard, N., Mende, S. B., Frey, H. U., & Sigwarth, J. B. (2005). Simultaneous imaging of the reconnection spot in the opposite hemispheres during northward IMF. *Geophysical Research Letters*, *32*, L21104. https://doi.org/10.1029/2005GL024491

Pettigrew, E. D., Shepherd, S. G., & Ruohoniemi, J. M. (2010). Climatological patterns of high-latitude convection in the Northern and Southern Hemispheres: Dipole tilt dependencies and interhemispheric comparisons. *Journal of Geophysical Research*, *115*, A07305. https://doi.org/10.1029/2009JA014956

Pitout, F., Escoubet, C. P., Klecker, B., & Dandouras, I. (2009). Cluster survey of the middle altitude cusp: 2. Large-scale morphology. *Annales de Geophysique*, *27*(5), 1875–1886. https://doi.org/10.5194/angeo-27-1875-2009

Pitout, F., Escoubet, C. P., Klecker, B., & Rème, H. (2006). Cluster survey of the middle altitude cusp: 1. Size, location, and dynamics. *Annales de Geophysique*, *24*(11), 3011–3026. https://doi.org/10.5194/angeo-24-3011-2006

Pitout, F., J-M Bosqued, D., Alcaydé, W. F., & Denig, H. R. (2001). Observations of the cusp region under northward IMF. *Annales de Geophysique*, *19*(10/12), 1641–1653. https://doi.org/10.5194/angeo-19-1641-2001

Reiff, P., Hill, T., & Burch, J. (1977). Solar wind plasma injection at the dayside magnetospheric cusp. *Journal of Geophysical Research*, *82*(4), 479–491. https://doi.org/10.1029/JA082i004p00479

Rème, H., Aoustin, C., Bosqued, J. M., Dandouras, I., Lavraud, B., Sauvaud, J. A., et al. (2001). First multispacecraft ion measurements in and near the Earth's magnetosphere with the identical Cluster ion spectrometry (CIS) experiment. *Annales de Geophysique*, *19*(10/12), 1303–1354. https://doi.org/10.5194/angeo-19-1303-2001

Rosenbauer, H., Gruenwaldt, H., Montgomery, M. D., Paschmann, G., & Skopke, N. (1975). HEOS-2 plasma observations in the distant polar magnetosphere: The plasma mantle. *Journal of Geophysical Research*, *80*(19), 2723–2737. https://doi.org/10.1029/JA080i019p02723

Russell, C. T., Snare, R. C., Means, J. D., Pierce, D., Dearborn, D., Larson, M., et al. (1995). The GGS/POLAR fields investigation. *Space Science Reviews*, *71*(1–4), 563–582. https://doi.org/10.1007/BF00751341

Samsonov, A. A., Sibeck, D. G., Dmitrieva, N. P., Semenov, V. S., Slivka, K. Y., Šafránkova, J., & Němeček, Z. (2018). Magnetosheath propagation time of solar wind directional discontinuities. *Journal of Geophysical Research: Space Physics*, *123*, 3727–3741. https://doi.org/10.1029/2017JA025174

Scudder, J., Hunsacker, F., Miller, G., Lobell, J., Zawistowski, T., Ogilvie, K., et al. (1995). Hydra—A 3-dimentional electron and ion hot plasma instrument for the Polar spacecraft of the GGS mission. *Space Science Revolution*, *71*(1–4), 459–495. https://doi.org/10.1007/BF00751338

Shepherd, S. G. (2014). Altitude-adjusted corrected geomagnetic coordinates: Definition and functional approximations. *Journal of Geophysical Research: Space Physics*, *119*, 7501–7521. https://doi.org/10.1002/2014JA020264

Spreiter, J. R., Summers, A. L., & Alksne, A. Y. (1966). Hydrodynamic flow around the magnetosphere. *Planetary and Space Science*, *14*, 223–250. https://doi.org/10.1016/0032-0633(66)90124-3

Stenbaek-Nielsen, H. C., Wescott, E. M., Davis, T. N., & Peterson, R. W. (1973). Differences in auroral intensity at conjugate points. *Journal of Geophysical Research*, *78*(4), 659–671. https://doi.org/10.1029/JA078i004p00659

Taylor, J. R., Lester, M., Yeoman, T. K., Greenwald, R., Sofko, G., & Villain, J.-P. (1998). Ionospheric convection response to a northward turning of the interplanetary magnetic field on March 23, 1995 studied employing SuperDARN HF radar data. *Advances in Space Research*, *22*(9), 1289–1292. https://doi.org/10.1016/S0273-1177(98)00173-2

Trattner, K. J., Burch, J. L., Ergun, R., Fuselier, S. A., Gomez, R. G., Grimes, E. W., et al. (2016). The response time of the magnetopause reconnection location to changes in the solar wind: MMS case study. *Geophysical Research Letters*, *43*, 4673–4682. https://doi.org/10.1002/2016GL068554

Trattner, K. J., Fuselier, S. A., Petrinec, S. M., Yeoman, T. K., Mouikis, C., Kucharek, H., & Reme, H. (2005). Reconnection sites of spatial cusp structures. *Journal of Geophysical Research*, *110*, A04207. https://doi.org/10.1029/2004JA010722

Trattner, K. J., Mulcock, J. S., Petrinec, S. M., & Fuselier, S. A. (2007). Probing the boundary between antiparallel and component reconnection during southward interplanetary magnetic field conditions. *Journal of Geophysical Research*, *112*, A08210. https://doi.org/10.1029/2007JA012270

Tsyganenko, N. A. (1995). Modeling the Earth's magnetospheric magnetic field confined within a realistic magnetopause. *Journal of Geophysical Research*, *100*, 5599–5612. https://doi.org/10.1029/94JA03193

Tsyganenko, N. A. (2002a). A model of the near magnetosphere with a dawn-dusk asymmetry—1. Mathematical structure. *Journal of Geophysical Research*, *107*(A8), 1179. https://doi.org/10.1029/2001JA000219

Tsyganenko, N. A. (2002b). A model of the near magnetosphere with a dawn-dusk asymmetry 2. Parameterization and fitting to observations. *Journal of Geophysical Research*, *107*(A7), 1179. https://doi.org/10.1029/2001JA000220

Wescott, E. (1962). Magnetic activity during periods of auroras at geomagnetically conjugate points. *Journal of Geophysical Research*, *67*(4), 1353–1355. https://doi.org/10.1029/JZ067i004p01353

Wilder, F. D., Eriksson, S., & Wiltberger, M. (2013). Investigation of the interhemispheric asymmetry in reverse convection near solstice during northward interplanetary magnetic field conditions using MHD simulations. *Journal of Geophysical Research: Space Physics*, *118*, 4289–4297. https://doi.org/10.1002/jgra.50421

Wing, S., Newell, P. T., & Ruohoniemi, J. M. (2001). Double cusp: Model prediction and observational verification. *Journal of Geophysical Research*, *106*(A11), 25,571–25,593. https://doi.org/10.1029/2000JA000402